Geodesic Flow Fields in Geophysical Fields via Mathematical Morphology

B. S. Daya Sagar

Agenda

- Data Used
- Basic Techniques
- Segmentation of Sets and Functions through Multiscale Convexity Analysis
- Geodesic Flow Fields and Spectrum of Discrete Functions

1. Introduction

- In geophysics context, surfaces can be broadly categorized as time-dependent, or time-independent

- Examples of time-dependent surfaces: cloud fields, bathymetric fields, topographic surfaces of tidal regions

- Examples of time-independent surfaces: topographic surfaces of fluvial regions

- The retrieval of parameters from the changes in the forms of natural features is the study area in this work

- Mathematical morphology is appropriately applied as it is a mathematical tool which is of geometric relevance

1.1 Objectives

- To characterize geophysically relevant surfaces via:

  - Segmenting the surfaces into different regions,
 - Deriving a new metric from propagation of flow fields in the basins.
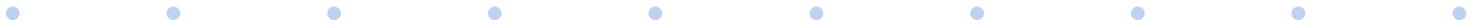
B. Water Surfaces – Synthetic Basin and Realistic Basin

- Three synthetic cases (Figs 1.5a-1.5c) with different internal topographic regions that replicate the (i) flat, (ii) undulated without channels, and (iii) undulated with channels conspicuous in topography are considered.

- In reality, these three cases mimic topography of shallow water regimes (eg., shallow lakes with flat bottom topography), bays and estuaries, and basins of floodplains and tidal environments.

- Fig 1.5a (Case 1) shows a simple basin with single inlet from which the water propagates uniformly within the mask set. With this assumption, oscillations in tidal levels and forcing will influence the whole tidal basin that is assumed to be flat.

- Fig 1.5b (Case 2) also assumes a single inlet but the water would first flow into channelized regions of uniform elevation followed by inland region. Hence, channelized sets and inlet are of different elevations.

Data Used [10/19]

- Nevertheless, in contrast to Fig 1.5a, flow fields in channelized sets in Fig 1.5b maintain orthogonality with the flow fields in nonchannelized sets. This is justifiable as flow propagation in channelized zones precedes flow propagation in nonchannelized regions.

- In Fig 1.5c (Case 3), the basin also shows a single inlet and water flow alternatively into channel region and into inland until the propagating waterfronts reach the basin boundary.
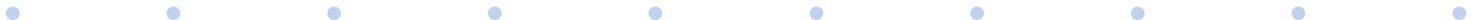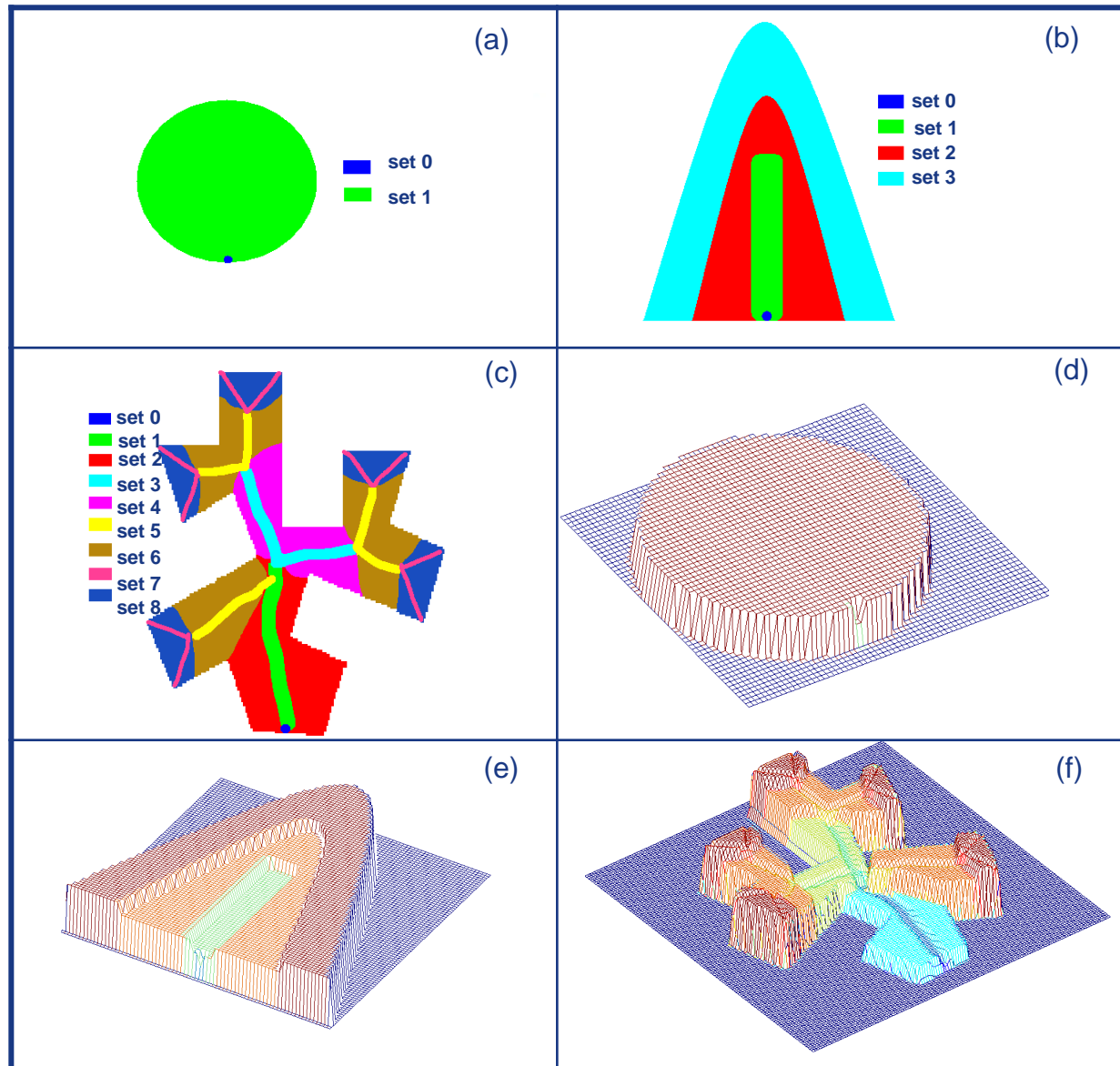
Fig 1.5 Tidal basins with different assumptions: (a) flat tidal basin, (b) tidal basin with a channelized and nonchannelized zones (multiple sets of topological significance), and (c) tidal basin with multiple sets, sets indexed with even and odd indexes, respectively, refer to channelized and nonchannelized zones. (d)–(f) 3D mesh representation of three synthetic tidal basin shown in (a)-(c).

Data Used [12/19]

- The Digital Bathymetric Map (DBM) of part of Central San Francisco Bay, acquired with multibeam system, has been utilized with permission from the United States Geological Survey (USGS).

- The coastal SFB's bathymetry which is of 4 m resolution and tide-corrected to mean low water level has been acquired through multibeam sonar system that provides echo sounders with 60 beams, collected in 1997 using a Simrad EM 1000 multibeam swath mapping system.

- The region of interest in SFB area, of size 512 x 480 pixels, covers approximately from 37°48′41″N to 37°51′34″N, and from 122°26′2″W to 122°29′28″W.

- As shown in Fig 1.6c, this region corresponds to a part at the mouth of the bay from which the tidal flow fields from the Golden Gate, located at the bottom left corner of Fig 1.6c, enter into the bay.

- It covers bathymetric depressions from the depth of -115 m to -14 m.

(a)

(b)

(c)

Fig 1.6 (a) 3D view of remote sensing data of Central San Francisco Bay, (b) bathymetry of Central San Francisco Bay, (c) bathymetry of inset of (b).

Data Used [16/19]

- USGS DEM data is a geospatial file format developed by USGS for storing raster-based DEM.
- In this work, the 10 m grid spacing DEM of coastal Santa Cruz region, downloaded from San Francisco Bay Area Regional Database (BARD) is used.
- Santa Cruz (California, US) is located on the northern edge of Monterey Bay, about 115 km south of San Francisco.
- At 10 m grid spacing, the Santa Cruz DEM is available as 7.5 minutes standard DEM format on Universal Transverse Mercator (UTM) projection on Zone 10 in North America.
- The case study region of interest in Santa Cruz, of size 346 x 654 pixels, covers approximately from 36°56′35″N to 37°00′00″N, and from 122°03′56″W to 122°05′38″W.
- Fig 1.9a depicts the 3D view of Santa Cruz while Fig 1.9b shows the DEM of a minor basin in Santa Cruz in grayscale. This basin has discharges flowing into the sea and covers elevation ranges between 1 m and 263 m.
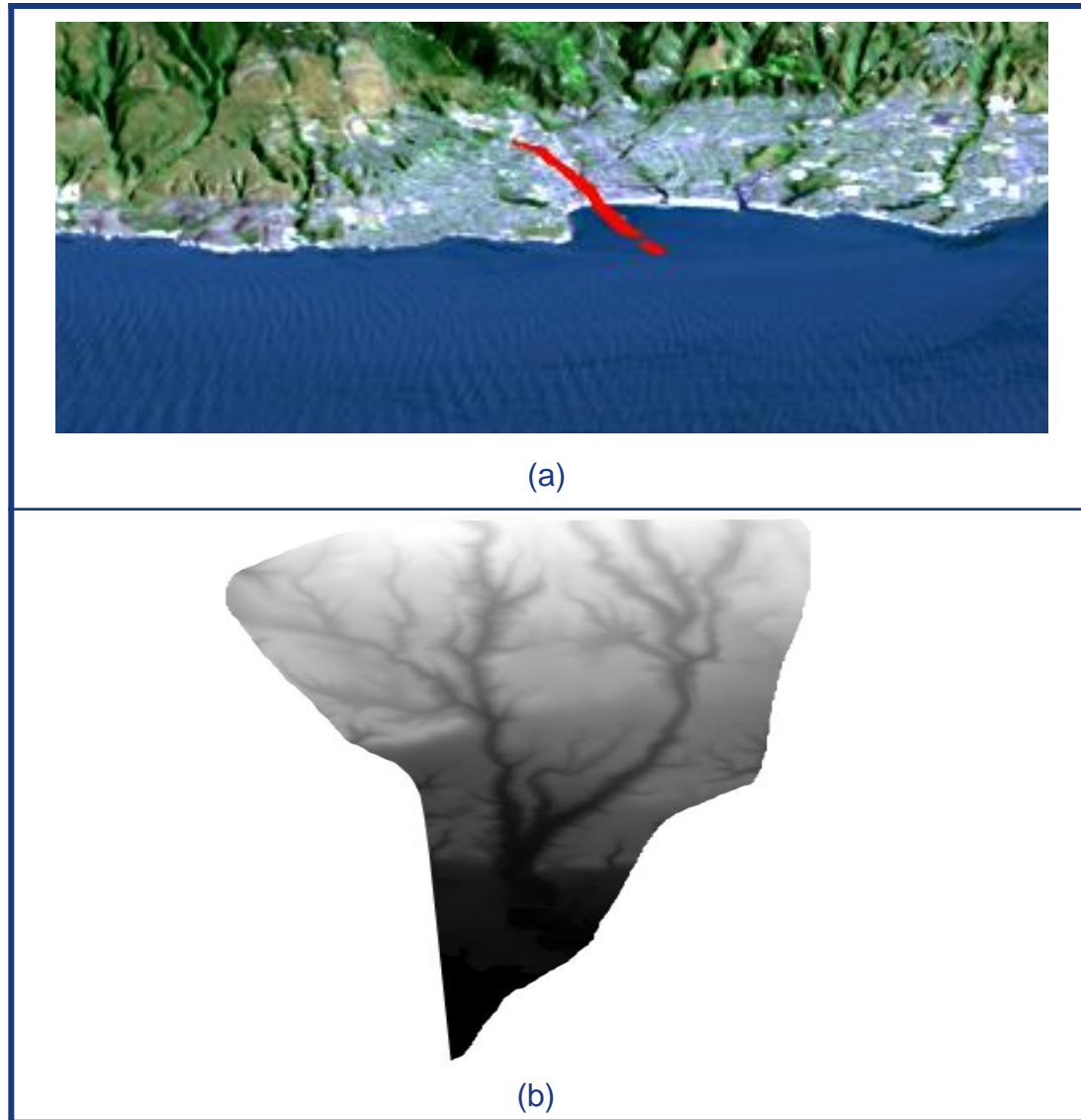
(a)

(b)

Fig 1.9 (a) 3D view of Santa Cruz, and (b) Digital elevation map of Santa Cruz.

Data Used [18/19]

- Topographic Synthetic Aperture Radar (TOPSAR) DEMs of Cameron Highlands and Petaling regions of Malaysia from Tay *et al.*(2007) are used.

- The Cameron Highlands study region encompasses 101°15′-101°20′E longitudes and 4°31′- 4°36′N latitudes, while the Petaling region is located between 101°37′-101°40′E and 2°59′-3°02′N.

- Cameron Highlands has rough physical relief and covers hilly terrain at altitudes between 400 m and 1800 m, while the Petaling region is a district located in Selangor which is comparatively flat with highest altitude of 215 m.

- Cameron Highlands DEM covers an area of 900 x 900 pixels with 10 m resolution, while Petaling DEM covers a region of 750 x 800 pixels with 5 m resolution.

- Based on the extracted channel network, these two DEMs are demarcated into 14 sub-basins: 7 from Cameron Highlands DEM (Fig 1.10a) and 7 from Petaling DEM (Fig 1.10b).
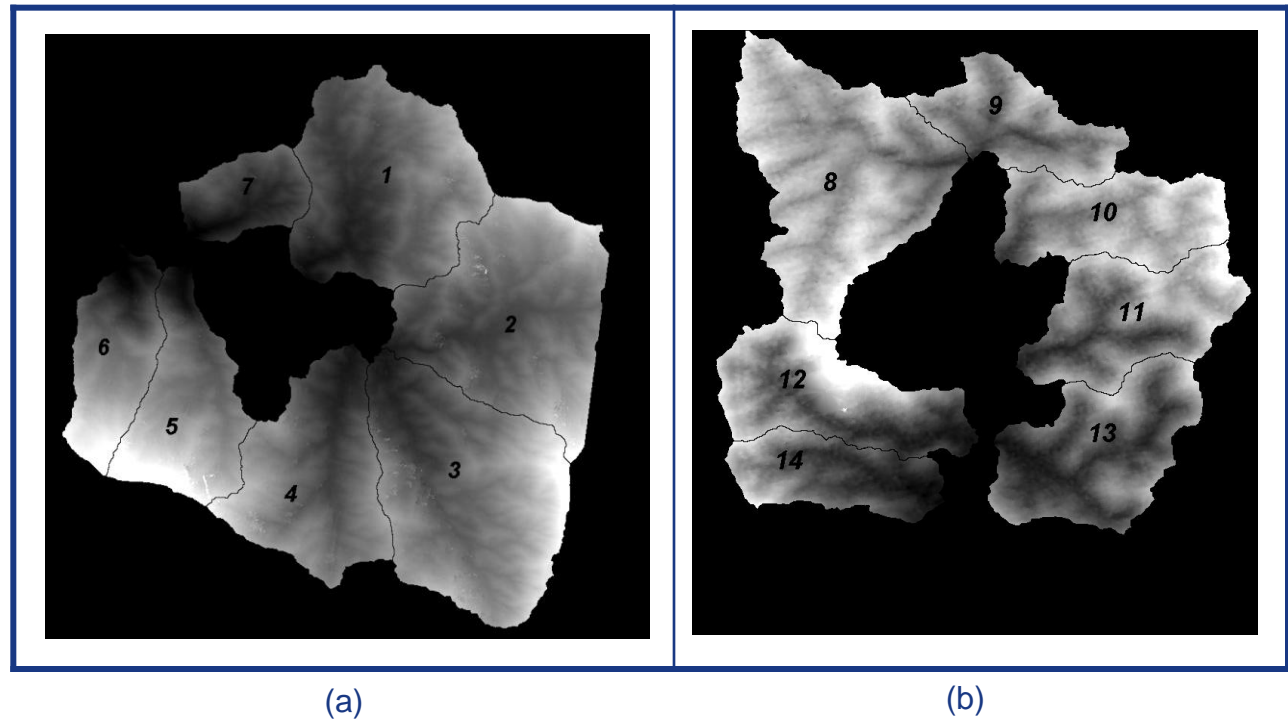

(a)   (b)

Fig 1.10 (a) 7 delineated sub-basins of Cameron Highlands DEM, and (b) 7 delineated sub-basins of Petaling DEM.

- The convex hull of MODIS cloud image (Fig 1.4a) is constructed (Fig 2.12i).

- Fig 1.4a is the input grayscale image, while Fig 2.12a-2.12h depict the closings computed using eight directional half planes. These eight directional half-plane closings include closings from the pair of left-right, upper-lower, $3\pi/4$, and $\pi/4$ directions.

- Finally, the point-wise minima of Fig 2.12a-2.12h result in the grayscale convex hull in Fig 2.12i.

- In Fig 2.13a-2.13d and Fig 2.13e-2.13h, the grayscale convex hulls obtained for the 25th, 50th, 75th, and 100th opened MODIS images (cloud-1 and cloud-2) are shown.

- It is observed that the convex hull decreases in size and encompasses smaller cloud area as the size of structuring element *B* increases.
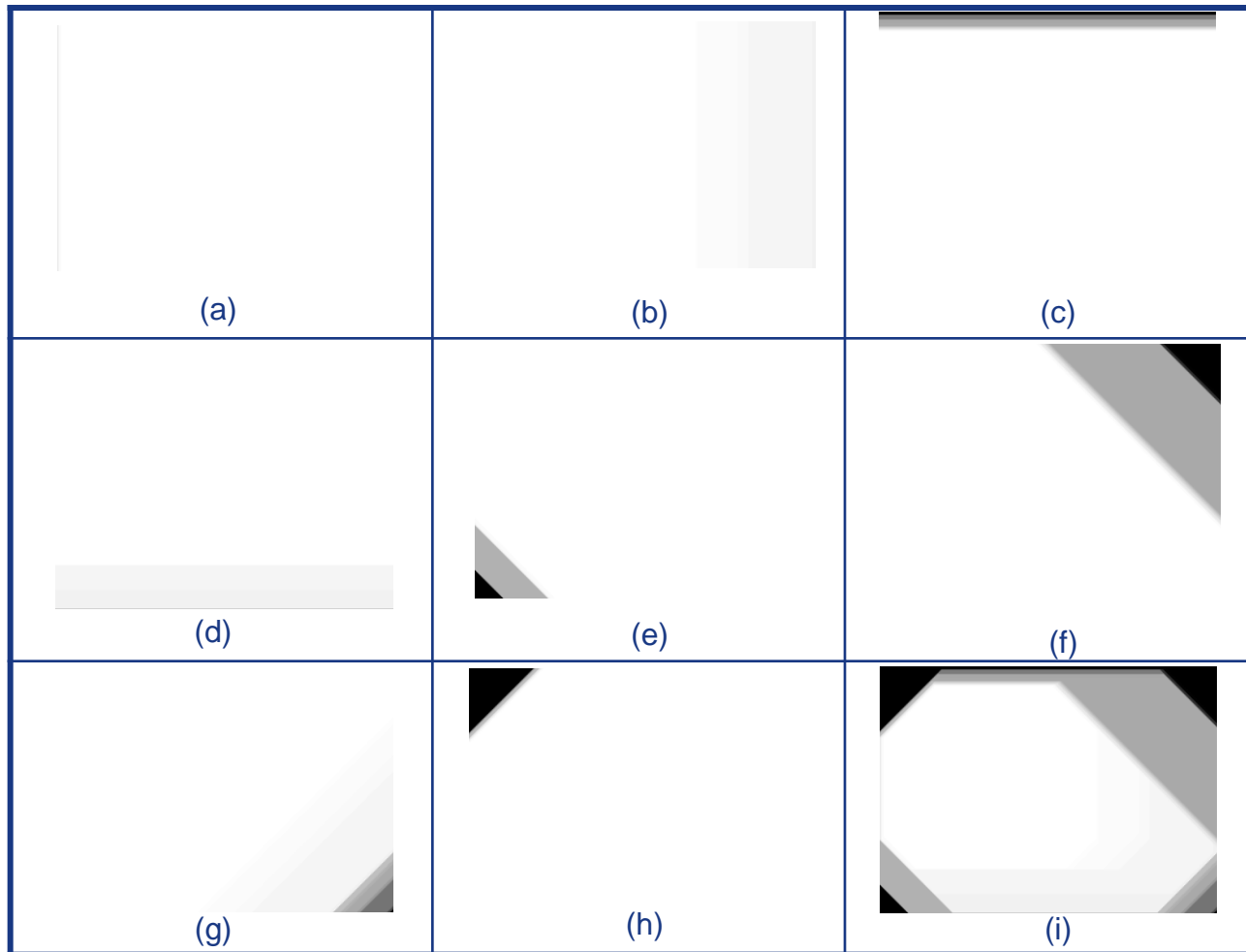
Fig 2.12 Convex hull generation of cloud function (Fig 1.4a) by half planes, based on the work of Soille (1998): (a) left-vertical half plane, (b) right-vertical half plane, (c) upper horizontal half plane, (d) lower horizontal half plane, (e) left half plane of orientation 3π/4, (f) right half plane of orientation 3π/4, (g) right half plane of orientation π/4, (h) left half plane of orientation π/4, and (i) intersection of all half-plane closings from Figs 2.12(a)– 2.12(h), resulting in grayscale convex hull of cloud function shown in Fig 1.4a.

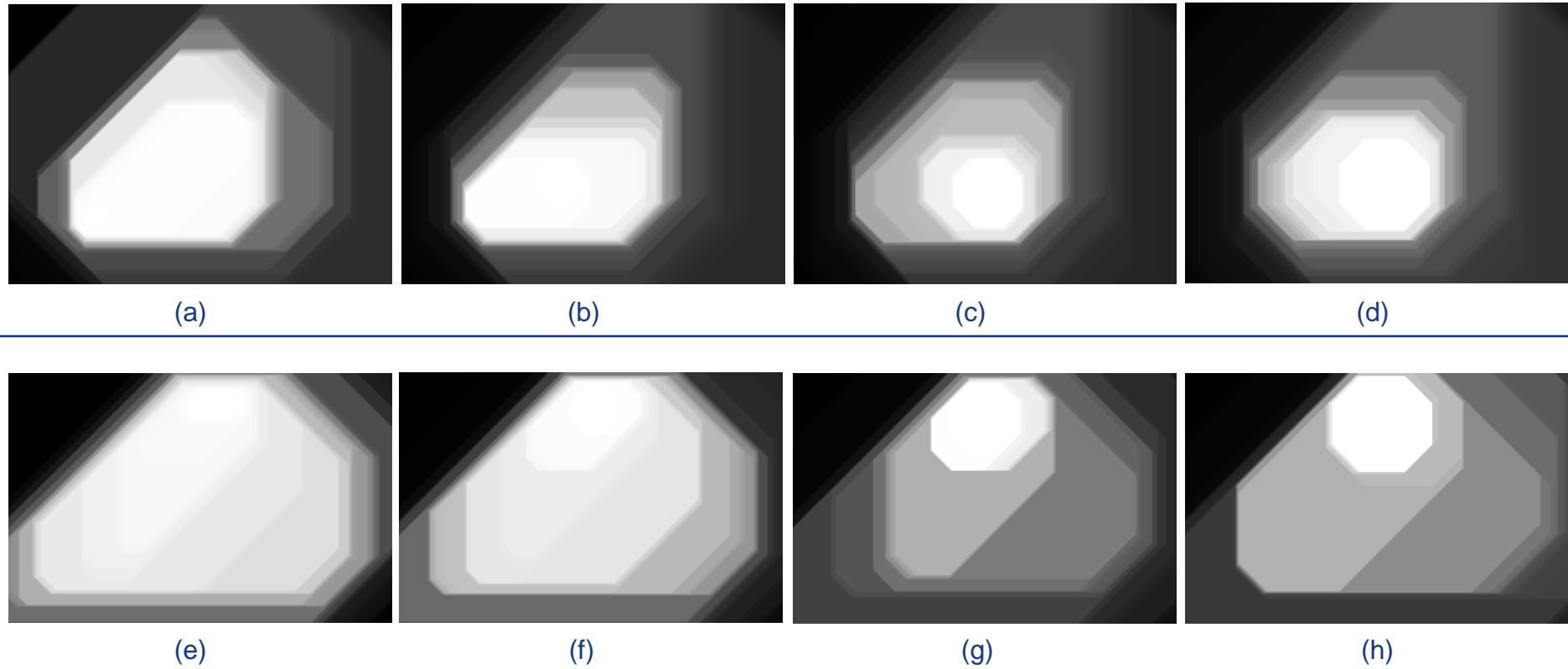(a)   (b)   (c)   (d)

(e)   (f)   (g)   (h)

Fig 2.13 (a-d) Convex hulls of 25th, 50th, 75th, and 100th opened versions of cloud-1, and (e-h) convex hulls of 25th, 50th, 75th, and 100th opened versions of cloud-2.

- A cloud field possesses a convex hull that acts as a super set to cloud field, and hence the area of the convex hull is greater than or equal to its corresponding cloud field.

- The area of cloud field (and also convex hull function) is the area computed as the sum of the gray values corresponding to the pixels of all spatial positions within a function

$$A(f) = \sum_{(x,y)} f(x,y) \text{ and } A[CH(f)] = \sum_{(x,y)} CH[f(x,y)] \qquad \textbf{(2.13)}$$

- It is obvious that the areas of multiscale cloud fields at decreasing resolution, together with areas of their corresponding convex hulls at decreasing resolutions, are in a decreasing trend, as shown in Fig 2.14a and 2.14b.
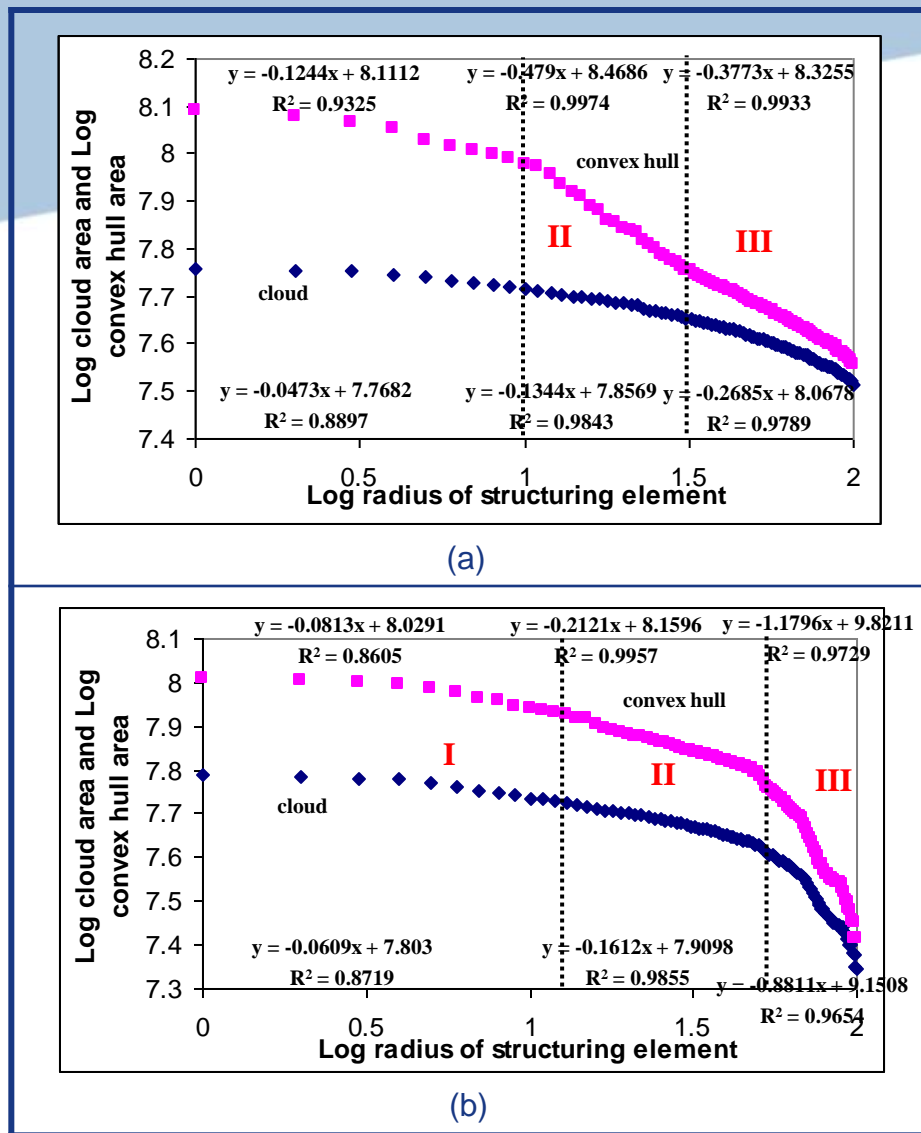
Fig 2.14 (a) Log-log graph between cloud area and convex hull versus corresponding radius of structuring element for cloud-1, (b) log-log graph between cloud area and convex hull versus corresponding radius of structuring element for cloud-2.

- The relationships between area of function and area of convex hulls are mathematically expressed as:

(1) $A(f) \geq A(f \circ 1B) \geq A(f \circ 2B) \geq \cdots \geq A(f \circ (N-1)B) \geq A(f \circ NB)$

(2) $A[CH(f)] \geq A[CH(f \circ 1B) \geq A[CH(f \circ 2B)] \geq \cdots \geq A[CH(f \circ (N-1)B)]$
$\geq A[CH(f \circ NB)]$, and

(3) $A(f \circ nB) \leq A[CH(f \circ nB)]$

for $n = 0,1,2,\cdots, N$

- From Figs 2.14a and 2.14b, it is observed that:
  - Areas of multiscale clouds and their corresponding convex hulls are merging at a point,
  - The multiscale clouds are the subfunctions of corresponding convex hulls,

- The relationship between the areas of convex hull and its cloud is shown on a log-log scale in Figs 2.15a and 2.15b.
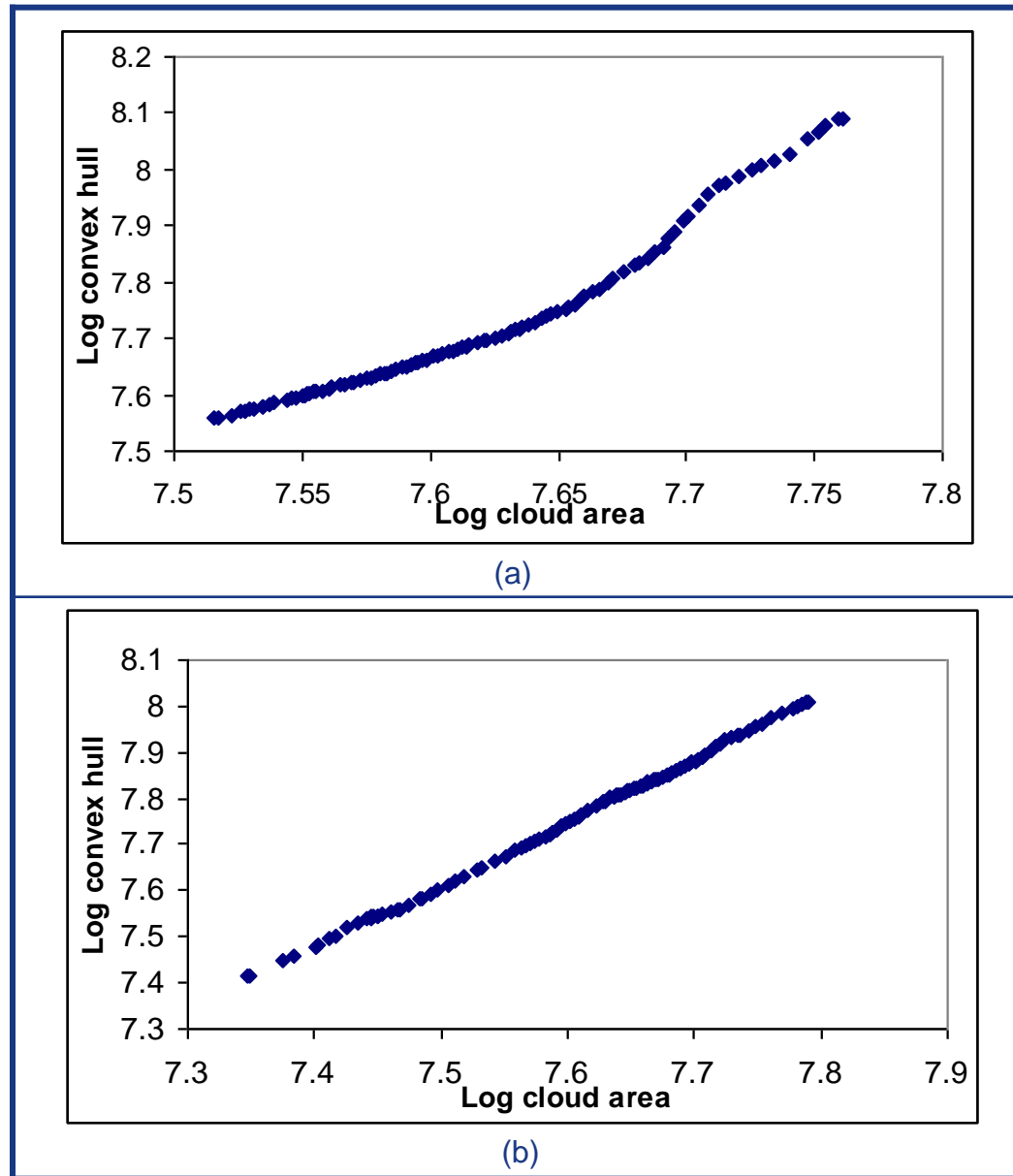
Fig 2.15 Log-log graph of convex hull versus cloud area for cloud-1, and (b) log-log graph of convex hull versus cloud area for cloud-2.

- To characterize clouds of varied spatial heterogeneities, the ratio between cloud area and its convex hull area is considered, and it could range between (0,1) as the area of a convex hull of a cloud is always greater than or equal to the area of its cloud.

- Hence, eq 2.14 can never exceed the unity value.

- Multiscale convexity measure $CM\{f \circ rB\}$ is defined as the ratio of areas under the function $A\{f \circ rB\}$ and its corresponding convex hull $A[CH\{f \circ rB\}]$:

$$CM\{f \circ rB\} = \frac{A\{f \circ rB\}}{A[CH\{f \circ rB\}]} \qquad (2.14)$$

Segmentation of Sets and Functions through Multiscale Convexity Analysis [28/32]

- To achieve appropriate segmentation process, changes that occur across multiscale cloud fields and their corresponding convex hulls are recorded in terms of areas.

- By using eq 2.14, the convexity measures at corresponding resolutions are estimated by taking the ratio of areas of cloud fields and areas of corresponding convex hulls.

- These convexity measures computed for cloud-1 and cloud-2 are plotted as a function of the resolution imposed due to multiscale opening, as shown in Figs 2.16a and 2.16b.
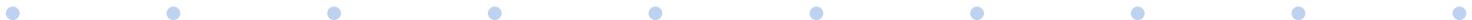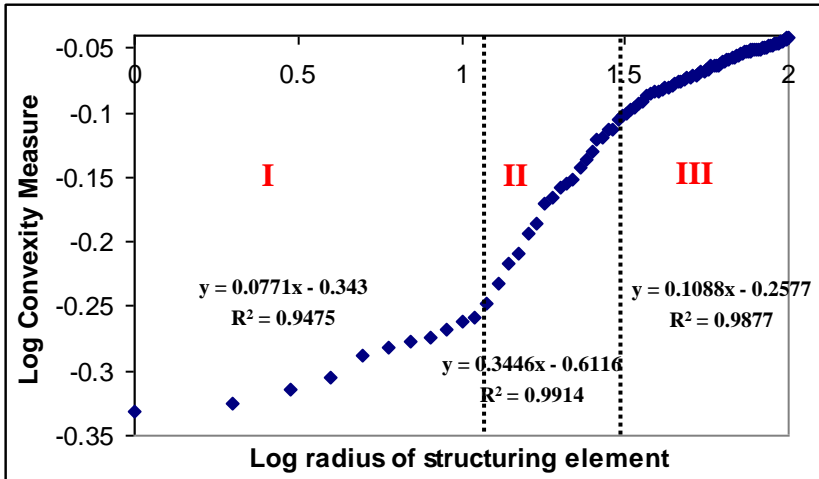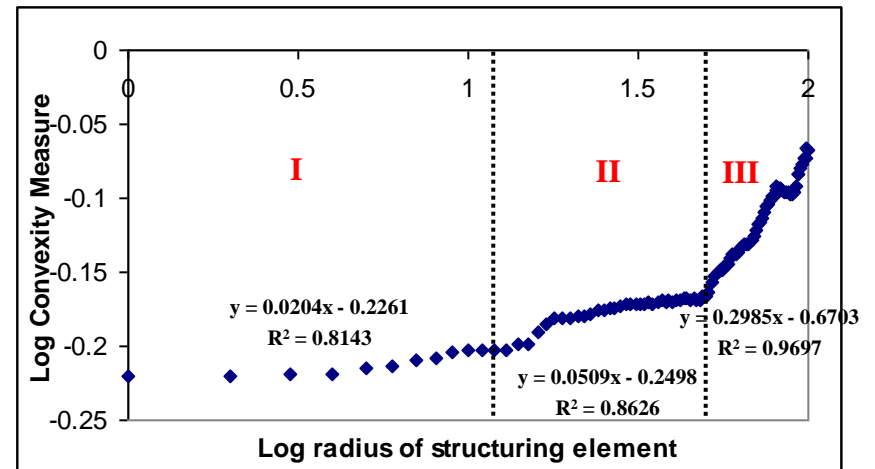
Fig 2.16 (a) Log-log graph between convexity measure with increasing radius of structuring element for cloud-1, and (b) log-log graph between convexity measure with increasing radius of structuring element for cloud-2.

Segmentation of Sets and Functions through Multiscale Convexity Analysis [30/32]

- From Figs 1.6a-1.6b, it is observed that there exist three different morphological regions.

- These crossover scales/radii are observed, for cloud-1, at scales or radii of structuring element of 1, 12, 32, and 100.

- In the middle region of cloud-1 (i.e., 12th cycle of opening to 32nd cycle of opening), the rate of change in convexity measure across resolutions is observed more than that of inner and external portions of cloud field.

- As a basis to categorize the cloud field, the convexity measure pattern across scales is thus divided into three groups. Group 1 – c.m. corresponding to s.e. from n =1 to 11, Group 2 – from n = 12 to 31, and Group 3 – from n = 32 to 100.

- Hence, Group 2 exhibits a higher rate of change, followed by Group 3 showing a moderate of change, and lastly Group 1 gives the slowest rate of increment, across multiple resolutions.

Segmentation of Sets and Functions through Multiscale Convexity Analysis [31/32]

- Based on the segregated phases shown in Figs 2.16a and 2.16b, Figs 2.17a and 2.17c are generated.

- It is observed that regions embedded within the segmented zones have different degrees of spatial homogeneities (Fig 2.17b).

- These classes for cloud-1 and cloud-2 are separated by choosing an "opening level" of image that changes abruptly, which can be observed from the graphs in Figs 2.16a and 2.16b.

- Shape-based segmentation of clouds has hitherto received little attention. Thus, the proposed method of segmenting cloud into regions of morphologic significance would provide a new insight. Regions within a cloud can be classified/categorized based on their general morphological constitutions and furthermore could be linked according to their potential to yield precipitation.

(a)

(b)

(c)

(d)

Fig 2.17 (a) Colour-coded binarized (by choosing threshold gray level value 128) cloud-images at three threshold-opening cycles superimposed on binarized original cloud-1 colour-coded with green, (b) boundaries of 12th, 32nd, and 100th opened cloud-1 images and 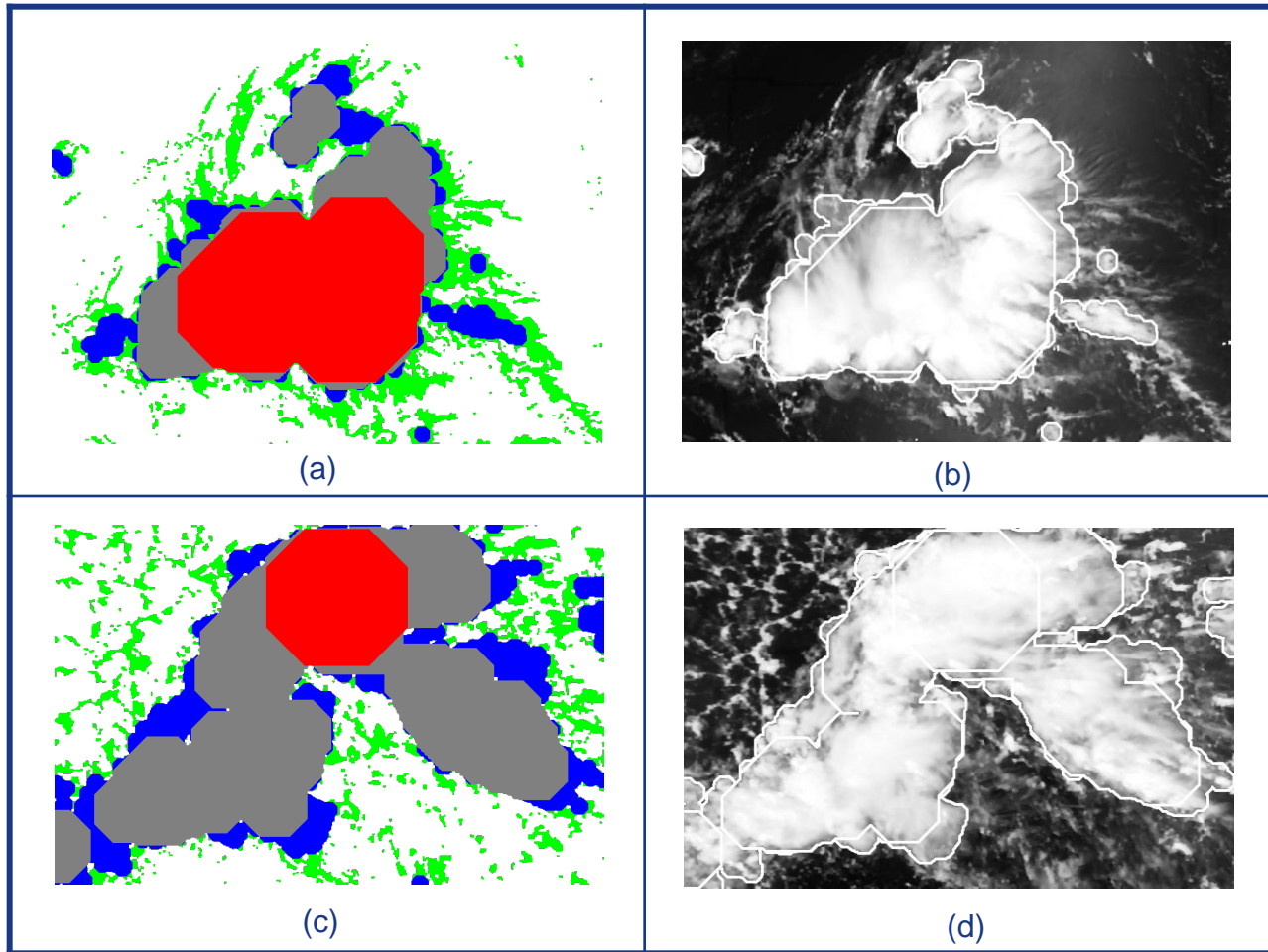thresholded original cloud-1 superimposed on the original cloud image, (c) colour-coded binarized (by choosing a threshold gray level value 110) cloud-2 images at threshold-opening cycles superimposed on binarized cloud-2 colour-coded with green, and (d) boundaries of 12th, 49th, and 100th opened cloud-2 images and thresholded original cloud-2 superimposed on the original cloud image.

6. Morphological Complexity Measures [1/11]

- For surfaces of geophysical nature, complexity measures explain the possible links with the processes involved in the formation of the surface. Such complexity measures include fractal dimension, granulometric indices, fourier descriptors etc.

- Within a surface, there may exist several different regions with different spatial complexities.

- Following the segmented fractal and cloud function, the morphological complexity (also known as roughness indices, or spatial complexity) for each segmented zone is investigated.

- This study offers new insights to quantitative characterization of spatial objects such as trees, and also geophysical fields including clouds, rainfall, temperature, vegetation, elevations, and landscapes.
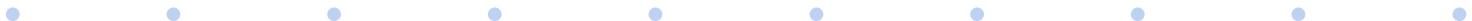
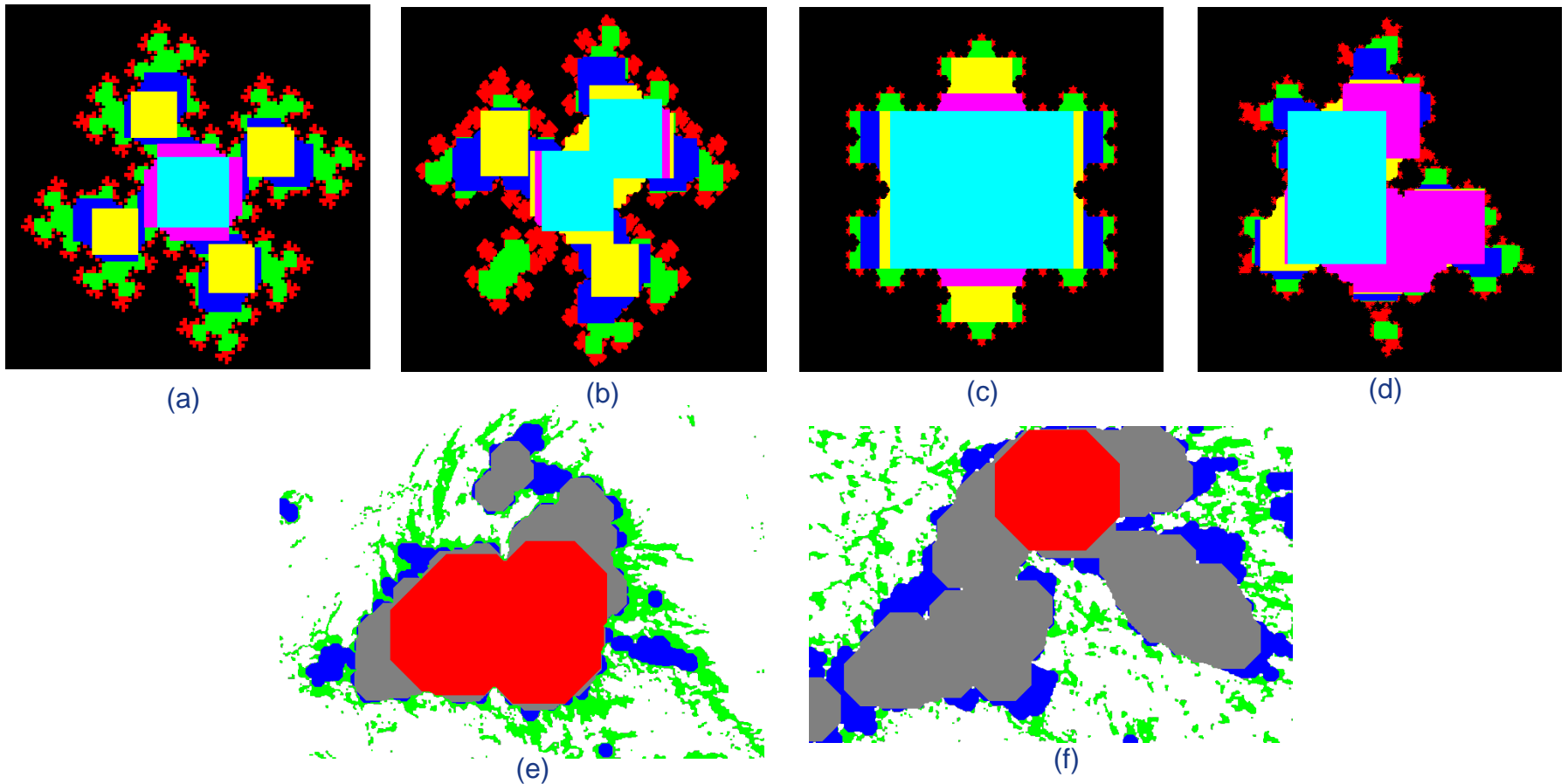**Fig 3.1 (a-d) Six zones segmented from deterministic and random Koch Quadric and Koch Triadic fractals, and (e, f) Four zones segmented from realistic MODIS clouds.**

- Each of the segmented six zones from fractals, and each of the four zones partitioned from cloud fields evidently possess different degrees of spatial complexity measures. A simple framework is provided here to compute the complexity measure of each segmented zone.

8. Geodesic Flow Fields and Spectrum of Discrete Functions [1/21]

- A framework to derive flow fields and spectrum in discrete functions particularly in digital topographic basins and cloud field is presented.

- Hereafter, "basin" refers to inland, tidal, floodplain, coastal, estuary regions, and digital topographies which include DEMs and DBMs, and "topography" refers to both surficial and bottom topographies.

- Through analysis of flow fields that are simulated via geodesic morphology, a new descriptor is generated that characterizes such discrete functions.

- This framework is demonstrated on (i) three synthetic basins, (ii) one realistic DEM, (iii) one realistic DBM, and (iv) two MODIS cloud fields.

- This study provides potentially invaluable insights to further investigate the travel-time flood propagation within basins of both fluvial and tidal systems, as well as the travel-time field and flow perturbations in cloud.

- Computation of this new descriptor involves the following five steps:

> **(i)** basin or cloud field in digital form representing topographic fluctuations or height variations, respectively, as an input

> **(ii)** hierarchical threshold decomposition of basin or cloud into sets

> **(iii)** proper indexing of these sets to determine the marker set(s) and its (their) corresponding mask set(s)

> **(iv)** perform geodesic propagation that provides basic flow field structures

> **(v)** finally to generate a new descriptor—geodesic spectrum to characterize basin or cloud

- The methodology involves two major steps: (i) decomposition of a function into threshold regions via threshold decomposition technique, and (ii) computation of geodesic dilations between marker (inlet) and mask (basin or threshold region).

- Consider a grayscale image represented by a nonnegative 2D sequence which assumes $J + 1$ possible intensity values: $j = 0,1,2,\ldots,J$. For instance, if the image is encoded as 8 bit/pixel, then $J = 255$. Threshold decomposed binary images or sets are obtained by thresholding at all possible intensity levels,

$$f_j(m,n) = \begin{cases} 1, f(m,n) \geq j, \\ 0, f(m,n) < j. \end{cases}$$

(5.1)

- The sets (f_j) form a sequence of sets that characterize f entirely, and are such that for any threshold elevations j and $j+1$ with $(j+1) \geq (j) \Rightarrow (f_{j+1}) \subseteq (f_j),$ for j ranging between 1 and J.

- By employing simple logical difference between the successive threshold-decomposed sets, marker set(s) and its (their) mask set(s) are further obtained according to $[f_j - f_{j+1} = S_i]$. Each thresholded set denoted by S_i is obtained by $f_j - f_{j+1}$, where $i, j = 1, 2, \cdots, J$.

- Fig 5.1 depicts threshold decomposition of an image f (e.g., digital topography) and isolation of threshold sets. In this figure, original image has maximum intensity level of $J = 4$. Threshold decomposed sets f_j with 1, 2, 3, 4, and 5 ($J + 1$) are, respectively, shown along with the isolated sets with index ranging from 1, 2, …, J. The sets are isolated by $f_j - f_{j+1}$.

Geodesic Flow Fields and Spectrum of Discrete Functions [5/21]

- Two sets, which are mask and marker sets, are considered.
- Let the mask set be denoted as S_{i+1} and marker set as S_i. To implement geodesic propagation with uniform velocity within a mask with certain boundary conditions from the marker set, (i) morphological dilation iteratively on with a structuring element B which is symmetric about the origin, and of primitive size 5×5 (e.g., Fig 5.2), (ii) logical intersection between the dilated marker and mask sets, and (iii) logical union of flow fields at respective discrete times, are employed.
- Fig 5.3 illustrates the result of intersecting the dilated marker set and mask set after four iterations.
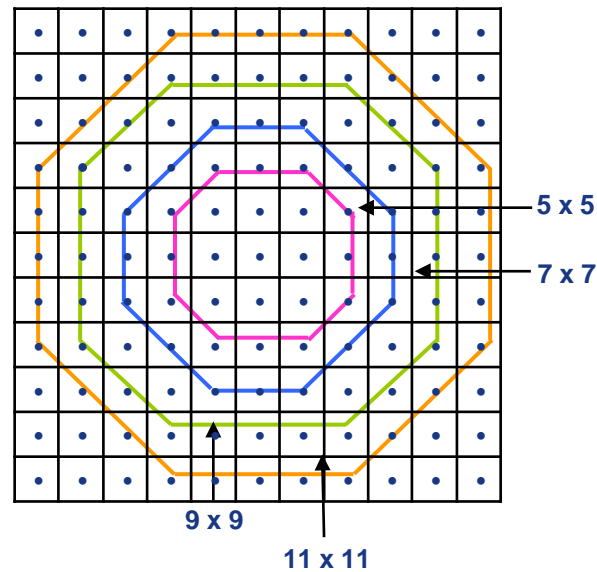
Fig 5.2 Octagonal symmetric structuring elements of various primitive sizes ranging from 5 × 5 to 11 × 11. These primitive sizes can be considered as *B* in the employed equations to simulate flow fields with various velocities.
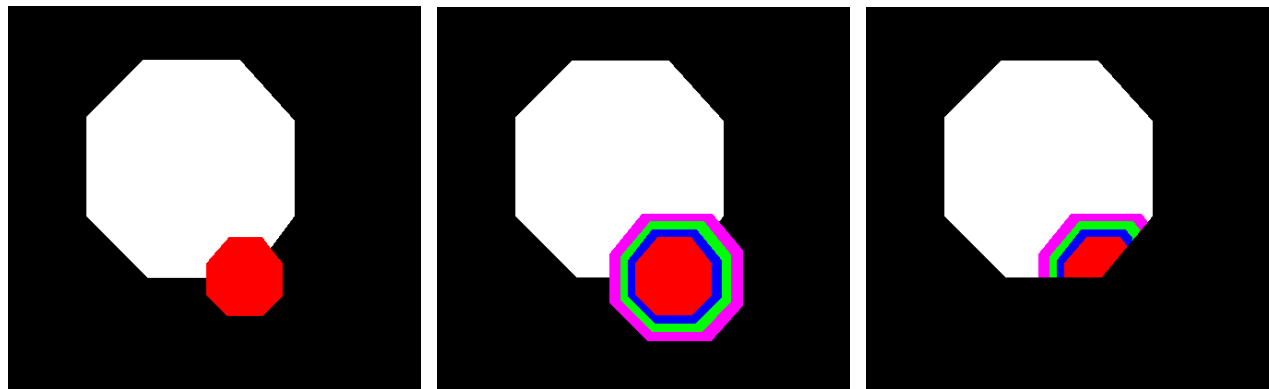
Fig 5.3 (a) Marker set S_i (in red) and mask set S_{i+1} (in white), (b) after iterative dilations up to fourth level superposed on the mask set S_{i+1}, and (c) the dilated marker set of four iterations intersected with mask set S_{i+1}.

- By taking synthetic basin Case 3 (Fig 1.5c) as example, the basin that consists of nine zones is decomposed into nine sets by specifying threshold elevations (values).

- These nine decomposed sets are designated with set-orders ranging from 1 to 9 (Fig 5.4). The union of these sets (f_j) and (S_i) satisfies the inclusion relationship (Maragos and Ziff, 1990) as shown in

$$f = \sum_{j=1}^{J} f_j \qquad\qquad f = \sum_{i=1}^{J} S_i$$

- For simplified representation, the decomposed sets thus obtained are denoted respectively as $S_i, S_{i+1}, S_{i+2}, \cdots, S_J$, with *i* ranging from 1 to *J* (Fig 5.4).

- Set S_1 denotes the inlet point. The set with immediate higher index acts as mask set to the marker set with preceding index.

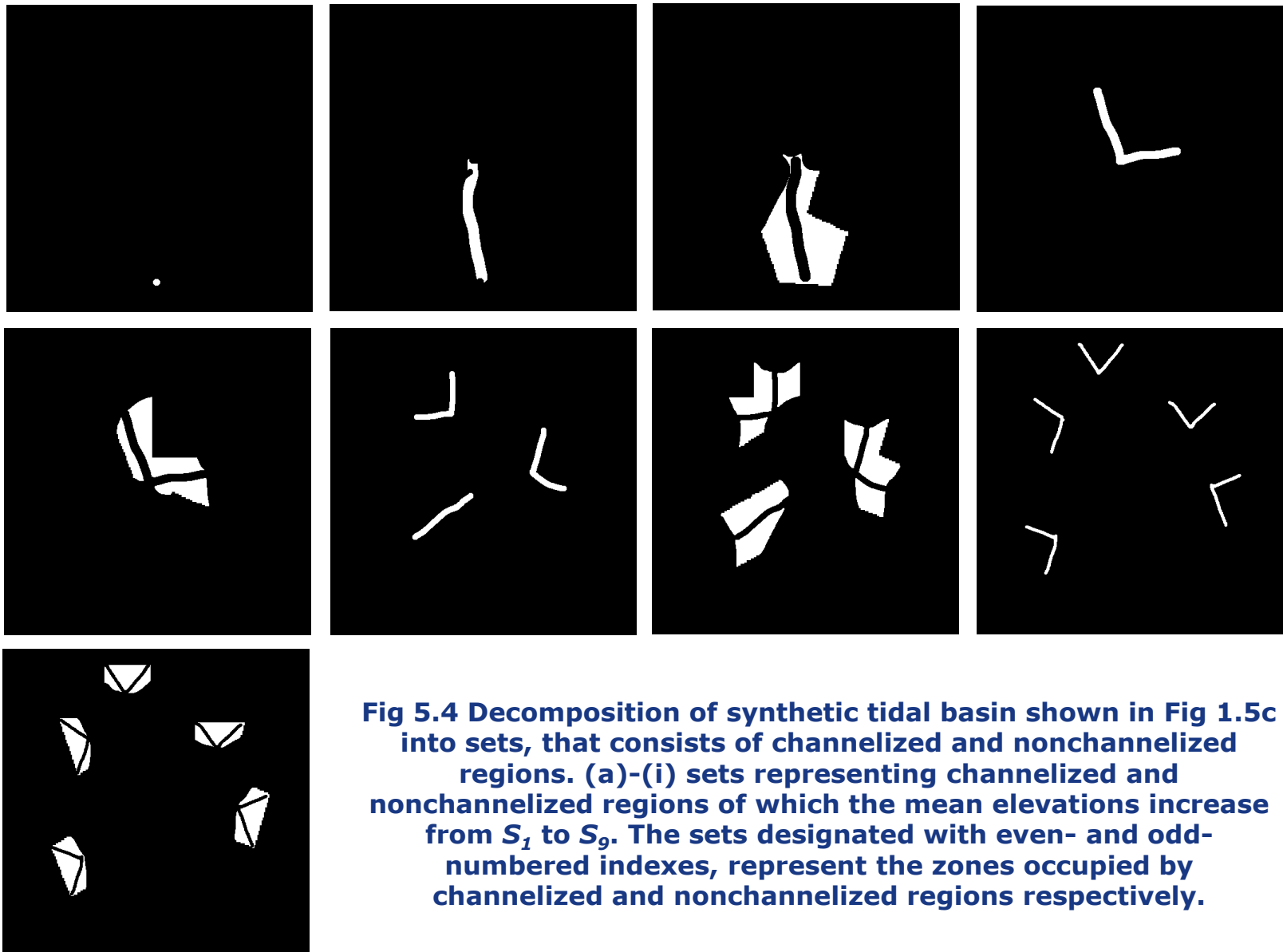**Fig 5.4 Decomposition of synthetic tidal basin shown in Fig 1.5c into sets, that consists of channelized and nonchannelized regions. (a)-(i) sets representing channelized and nonchannelized regions of which the mean elevations increase from S_1 to S_9. The sets designated with even- and odd-numbered indexes, represent the zones occupied by channelized and nonchannelized regions respectively.**

Geodesic Flow Fields and Spectrum of Discrete Functions [9/21]

- Geodesic morphological transformations (Lantuejoul and Maisonneuve, 1984) are adopted to simulate flow field propagation in discrete functions like basin and cloud field.

- James Sethian's (1999) level set theory and Jean Serra's (1982) random sets and mathematical morphologic concepts offer various transformations to simulate flow fields within basin with physical viability.

- To implement geodesic transformations, the basin is considered as a mask, and the inlet point (through which water flows into the basin during the high flood) is taken as a marker from which the flow propagates into the basin as the flood level increases.
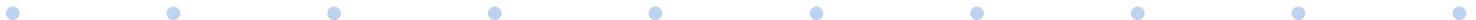
- The marker set is represented as S_i and mask set is denoted as S_{i+1}, followed by iterative morphological dilation on S_i with a structuring element which is of primitive size 5 × 5 and symmetric about the origin. Finally, to retrieve the flow fields at respective discrete time, logical intersection between the dilated marker set and mask set is performed, as given in eq 5.2:

$$(S_i \oplus nB) \bigcap (S_{i+1}) \qquad \textbf{(5.2)}$$

- In a flat basin where there is no distinction between channelized and nonchannelized regions in terms of elevations (e.g. Figs 1.5a, 1.5d), the total flow field can be defined in morphological terms as the intersections of gradients of successively dilated marker set with the mask set. nth-time step gradient between the successively dilated marker set is defined as

$$\partial^n(S) = [(S_i \oplus (n+1)B) \setminus (S_i \oplus nB)] \qquad \textbf{(5.3)}$$

- The total flow field in the simplest Case 1 (Figs 1.5a, 1.5d) can be achieved by following eq 5.4. In order to visualize the flow fields within the channelized and nonchannelized zones (or sets), a logical union operation is considered in the respective governing equations:

$$TB_{flow} = \bigcup_{\substack{n \geq 0 \\ i \geq 1}}^{\substack{J \\ N}} \{[\delta^n(S_i)] \cap S_{i+1}\} \qquad \textbf{(5.4)}$$

$$C_{flow} = \bigcup_{n=0}^{K} \{[\partial^n(S_1)] \cap S_{2i}\} \quad \textbf{and} \quad NC_{flow} = \bigcup_{n=0}^{N} \{[\partial^n(S_{2i})] \cap S_{2i+1}\}$$

$$C_{flow} = \bigcup_{n=K+1}^{P} \{[\partial^n(S_1)] \cap S_{2i}\} \quad \textbf{and} \quad NC_{flow} = \bigcup_{n=0}^{N} \{[\partial^n(S_{2i})] \cap S_{2i+1}\}$$

$$C_{flow} = \bigcup_{n=P+1}^{Q} \{[\partial^n(S_1)] \cap S_{2i}\} \quad \textbf{and} \quad NC_{flow} = \bigcup_{n=0}^{N} \{[\partial^n(S_{2i})] \cap S_{2i+1}\}$$

$$C_{flow} = \bigcup_{n=Q+1}^{N} \{[\partial^n(S_1)] \cap S_{2i}\} \quad \textbf{and} \quad NC_{flow} = \bigcup_{n=0}^{N} \{[\partial^n(S_{2i})] \cap S_{2i+1}\} \qquad \textbf{(5.5)}$$

(a)   (b)   (c)
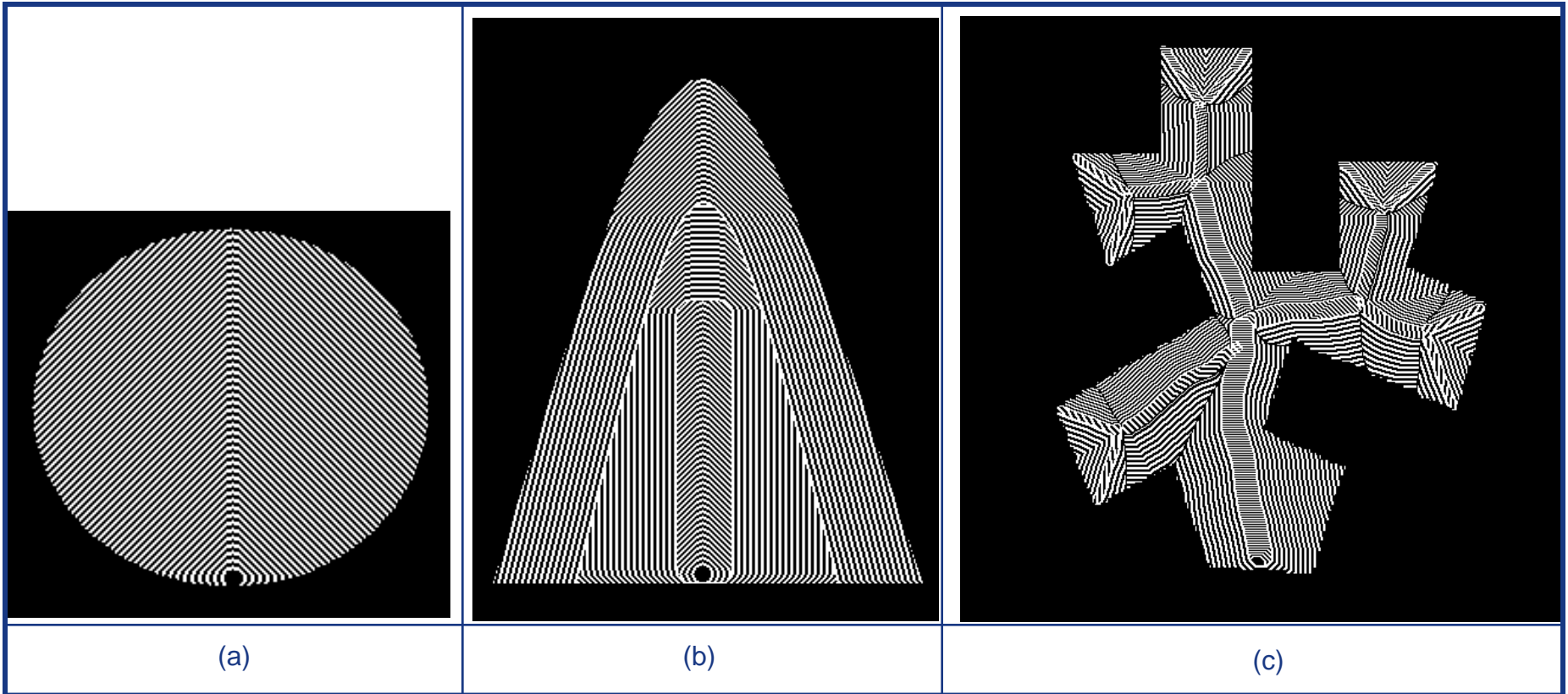
Fig 5.5 (a) Flow fields with isotropic propagation, (b) isotropic flow fields, and orthogonality between the flow fields of channelized and nonchannelized zones is obvious, and (c) flow fields within the tidal basin.
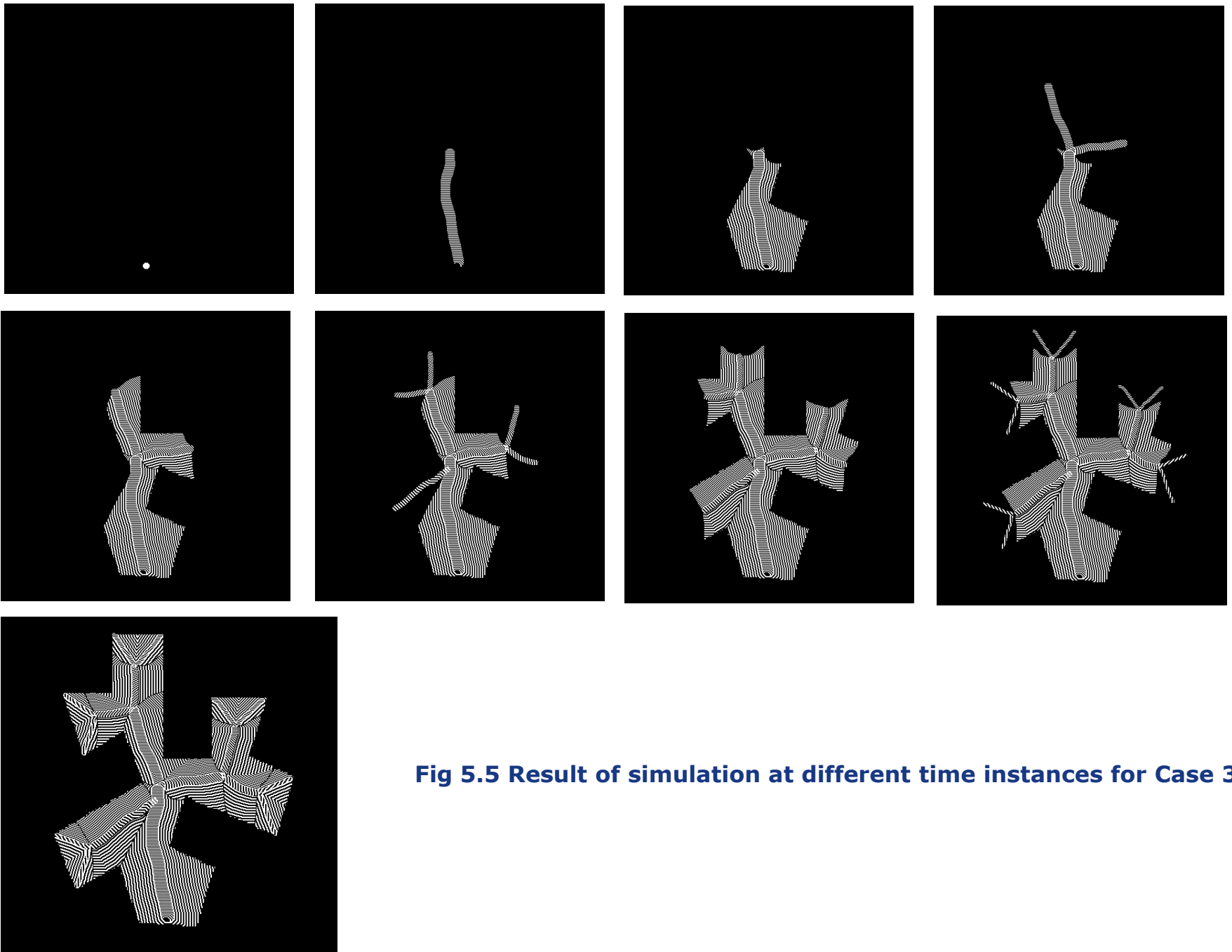
Fig 5.5 Result of simulation at different time instances for Case 3.
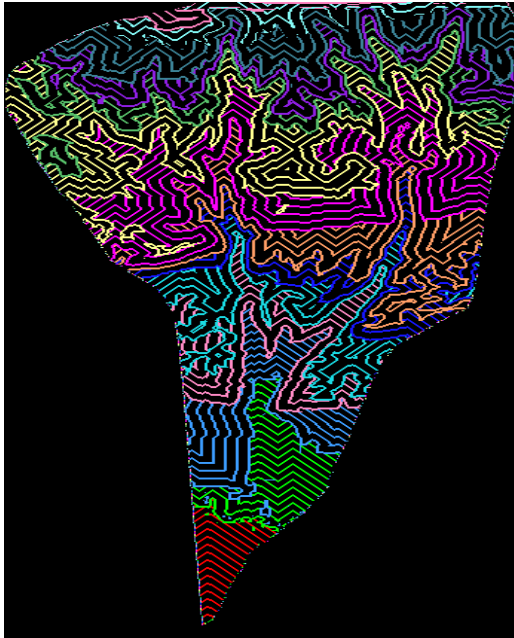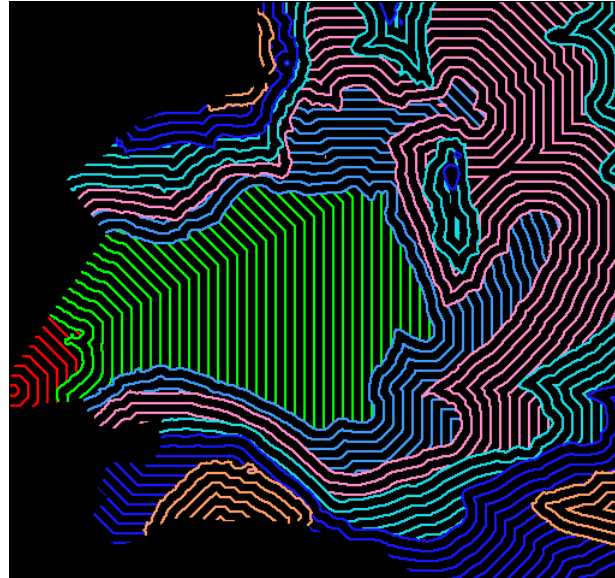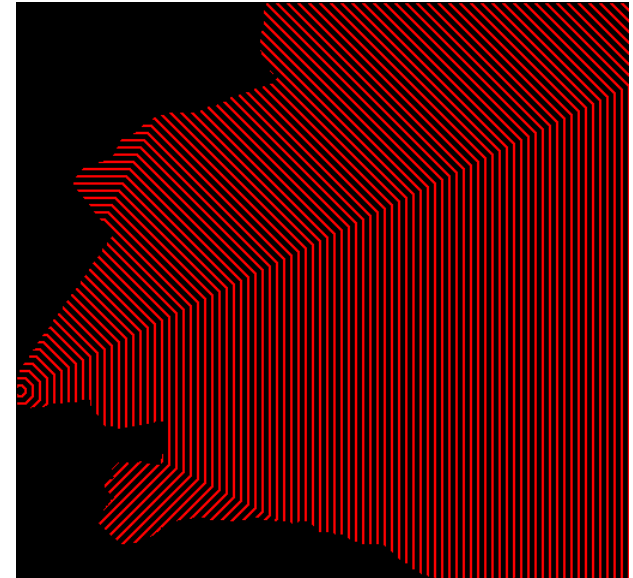
Fig 5.6 (a) Flow field simulated on Santa Cruz DEM by using octagon structuring element, **(b)** flow field simulated on San Francisco Bay bathymetry by using octagon structuring element, and **(c)** flow field simulated on San Francisco Bay without considering bathymetry.

(a)   (b)
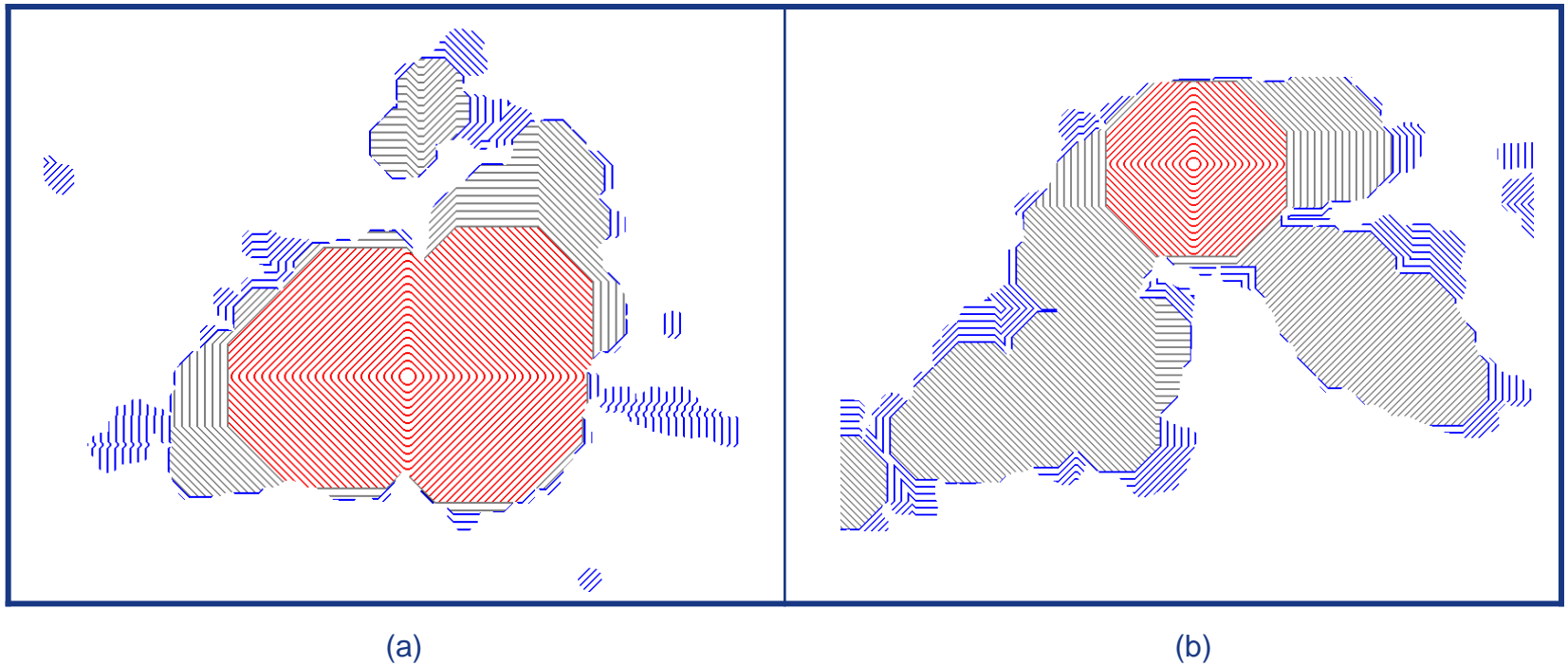
Figure 5.7 (a) Simulated flow fields of MODIS cloud-1, and (b) simulated flow fields of MODIS cloud-2.

- A new morphological descriptor based on geodesic flow spectrum to explain inter zone morphologic relationship is proposed.

- Area of each set decomposed from discrete functions (or threshold elevation regions, TER), denoted as $A[S_i]$ is estimated according to $\sum_{x,y} S_i(x,y)$, and area of all the TERs $(A[\sum_{i=1}^{J} S_i])$ is estimated as $\sum_{i=1,x,y}^{J} S_i(x,y)$.

- Geodesic flow spectrum is the area embedded between the successive flow fields. This spectrum of decomposed elevation set (S_i) with structuring element B of radius n is denoted as $GS_{S_i(n,B)}$, and is defined as follows: .

$$GS_{S_i(n,B)} = A[(S_i \oplus (n+1)B) \bigcap (S_{i+1})] - A[(S_i \oplus (n)B) \bigcap (S_{i+1})]$$

- The decomposed set-wise entropy based on total area of all the sets, as decomposed from the function, is defined as:

$$H/(S_i, B) = -\sum_{n=0}^{N} P_{S_i(n,B)} \log P_{S_i(n,B)}$$

- This geodesic spectrum forms a one-dimensional path support of different TERs and adjacent TERs which could help to better understand the morphological structures of the basins.

- Potentially valuable insights and links with instantaneous unit hydrograph can be further explored. These functions provide general geodesic distribution pattern, which further implies that geodesic function of each TER is in someway similar to geomorphic width function.

Table 5.1 Details of synthetic and realistic digital topographies considered with their gray levels' and corresponding elevation/or depth ranges, and entropy values estimated for each threshold elevation/depth decomposed set of each digital topographic basin.

Case	Type	Dyn Range	No. Dec	Gray value Range	Elevation Range (m)	Used SE	No. Flow Field	Entropy
Case 1	Synthetic	0-1	1	0-1	0-1	Rhombus	113	2.014109
Case 2	Synthetic	0-3	3	0-1	0-1	Rhombus	97	0.335195
				1-2	2		39	0.666177
				2-3	3		46	0.987891
Case 3	Synthetic	0-7	8	0-1	0-1	Rhombus	108	0.174197
				1-2	2		39	0.421361
				2-3	3		67	0.136298
				3-4	4		32	0.272975
				4-5	5		90	0.164091
				5-6	6		29	0.562372
				6-7	7		14	0.122462
				7-8	8		17	0.332124

SF-Bay	Bathymetry	0-255	7	0-33	-115 to -106	Octagon	34	0.048562
				34-59	-105 to -91		146	0.593921
				60-100	-90 to -68		57	0.365169
				101-150	-67 to -46		57	0.604285
				151-201	-45 to -27		23	0.304051
				202-233	-26 to -15		56	0.321996
				234-255	-14 to 0		22	0.120496
SC-Topo	Topography	0-255	14	0-1	0-1	Octagon	60	0.084891
				2-14	2-14		65	0.150806
				15-34	15-35		36	0.163969
				35-65	36-67		36	0.147204
				66-85	68-88		32	0.131617
				86-102	89-105		31	0.11603
				103-124	106-128		35	0.190187
				125-157	129-162		73	0.239391
				158-182	163-188		27	0.288595
				183-197	189-203		12	0.130263
				198-212	204-218		17	0.129661
				213-239	219-246		18	0.104142
				240-252	247-260		11	0.078623
				253-255	261-263		7	0.024073

Table 5.2 Details of MODIS cloud fields considered with their number of flow fields and entropy values estimated for each segmented zone.

Case	Dyn Range	No. Dec	Segmented zone	SE Used	No. Flow Field	Entropy
MODIS-cloud 1	0-255	3	Inner	Disc	141	2.0782
			Middle		105	1.873986
			Outer		175	1.769853
MODIS-cloud 2	0-255	3	Inner	Disc	73	1.81023
			Middle		338	2.422433
			Outer		100	1.50687
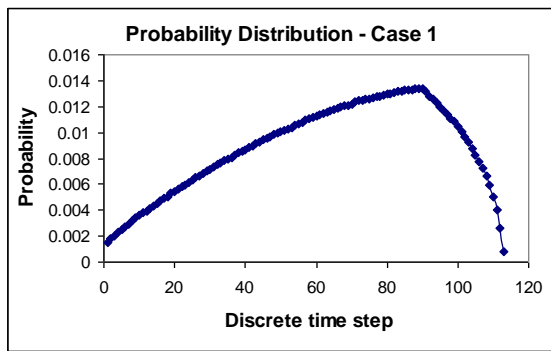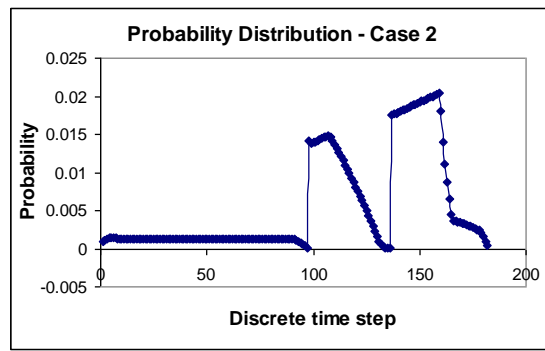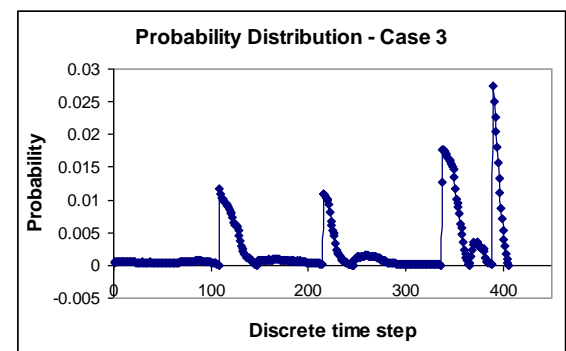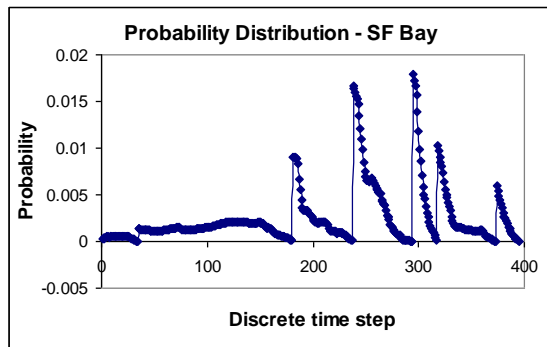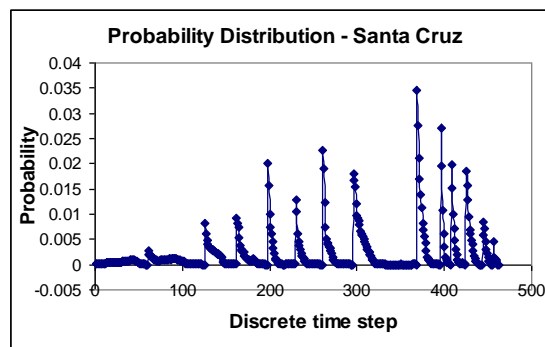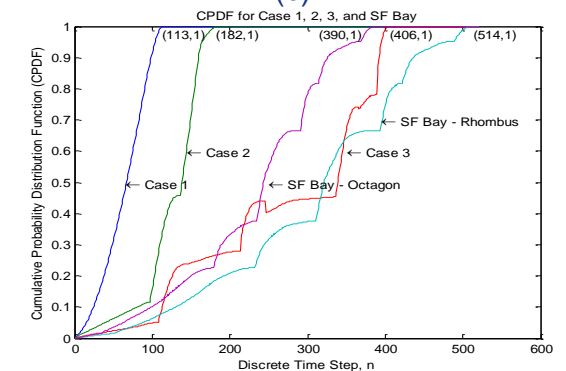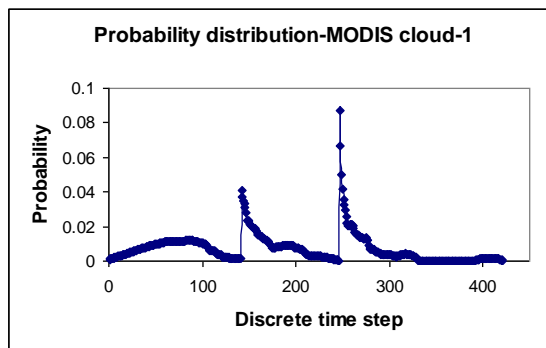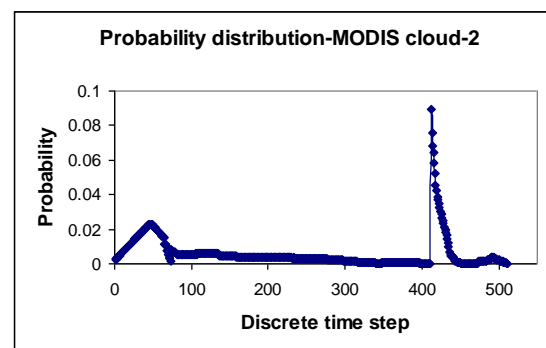
Figure 5.8 Probability of estimated area flooded/propagated at each discrete time step.

9. Investigation of Time-varying Phenomena

- Interpolation is a technique used to generate intermediary images between the initial and final images (Beucher, 1998).

- Various tools are available to create interpolation, including classical arithmetic interpolation, morphing techniques, and weighting functions.

- However, morphological interpolation is adopted here as it better preserves the topological (connectivity) properties of the images (Mathematical Morphology and Image Interpolation (No date). *The Image Interpolation Page* [Online]).

- Iwanowski and Serra (1999) defined morphological interpolation between two sets (e.g., set *X* and set *Y*) as,

$$M(X,Y) = \{(X \oplus B)(Y \ominus B)\} \qquad \textbf{(6.1)}$$
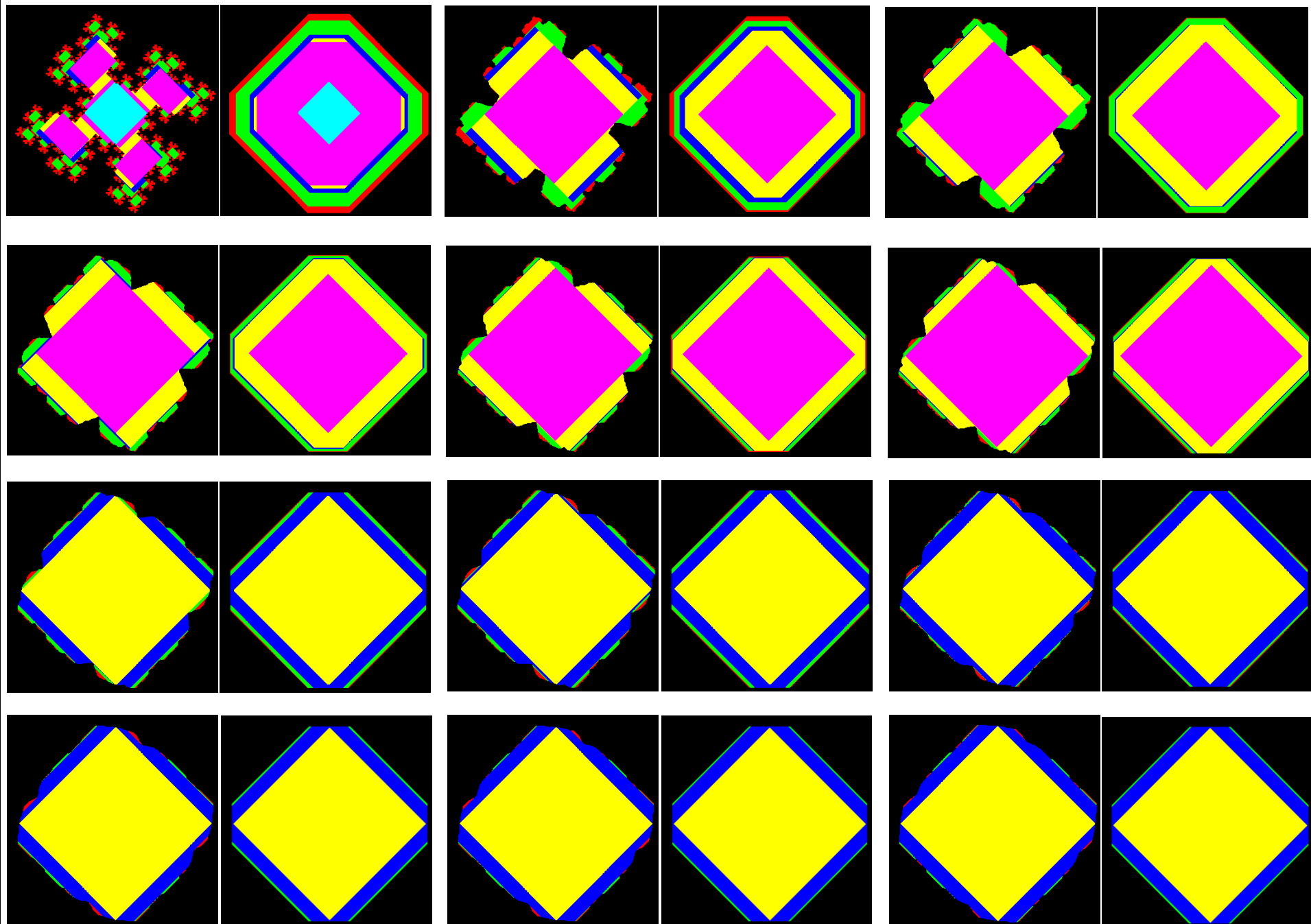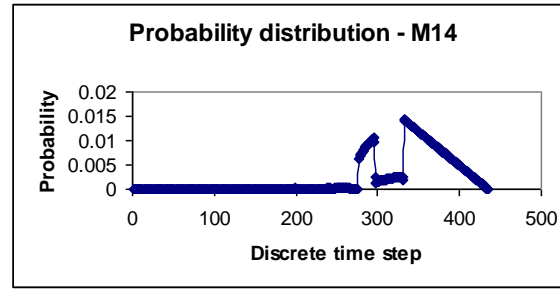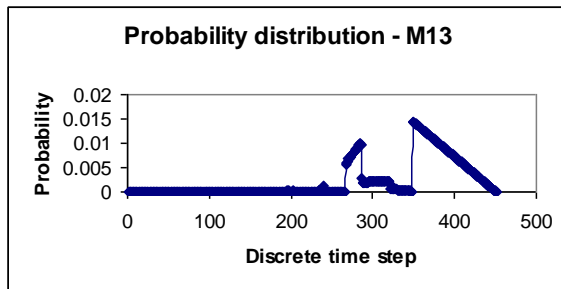
Fig 6.7 Probability of estimated area flooded at each discrete time step, from (a) M_1 to (o) M_{15}.

• Besides, the zone-wise entropy for each time-varying fractal, with respect to total area of all the zones in the fractal, is defined as:

$$H/(Z_j, B) = -\sum_{n=0}^{N} P_{Z_j(n,B)} \log P_{Z_j(n,B)}$$
(6.8)

Table 6.2 Details of time-varying fractal sets considered with their crossover scales determined, number of decomposed zones, number of geodesic flow fields obtained, and entropy values estimated.

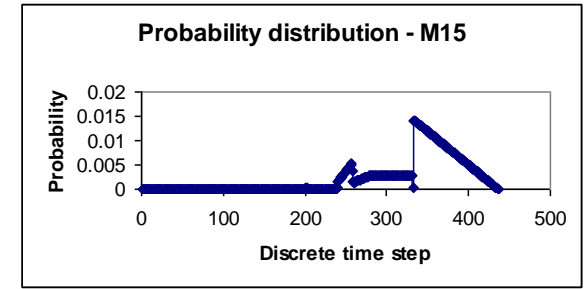| Fractal	Crossover scales	No. dec	No. flow field	Entropy	Fractal	Crossover scales	No. dec	No. flow field	Entropy
M_1	5, 12, 16, 20, 31	6	241 9 8 32 41 33	0.711406 0.259817 0.108419 0.221616 0.636800 0.303360	M_9	14, 58, 99	4	239 8 22 100	0.042599 0.035425 0.446141 1.523238
M_2	14, 30, 53, 71	5	239 22 24 31 72	0.162451 0.263529 0.200571 0.577769 0.967334	M_{10}	15, 58, 100	4	239 28 54 101	0.035253 0.039616 0.494237 1.527305
M_3	13, 30, 56, 77	5	238 18 24 35 78	0.069039 0.250096 0.042545 0.672546 1.077001	M_{11}	15, 58, 100	4	239 28 55 101	0.028256 0.028346 0.533474 1.519841
M_4	14, 28, 59, 82	5	239 13 24 32 83	0.067557 0.176975 0.054788 0.622612 1.173347	M_{12}	16, 59, 101	4	240 27 55 102	0.024655 0.029049 0.541056 1.519717
M_5	14, 26, 60, 90	5	238 15 23 41 91	0.054754 0.119036 0.029971 0.525751 1.349119	M_{13}	16, 60, 101	4	239 27 82 103	0.020976 0.014666 0.568972 1.530993
M_6	15, 25, 61, 95	5	239 12 21 41 96	0.066291 0.086667 0.029225 0.440837 1.450388	M_{14}	16, 61, 102	4	240 36 55 104	0.010041 0.021141 0.554284 1.532161
M_7	14, 61, 97	4	239 9 18 100	0.051704 0.082322 0.373257 1.544069	M_{15}	11, 102	3	239 93 104	0.005831 0.651933 1.530318
M_8	15, 61, 98	4	240 6 19 101	0.059185 0.070256 0.389670 1.537758					

Investigation of Time-varying Phenomena

- To characterize the evolving cloud fields, segmentation for each cloud field (i.e., from f_1 to f_{15}) is first performed via multiscale convexity measure, and based on the decomposed zones, complexity measures for decomposed zones for each evolving cloud function are computed; furthermore flow field propagation is simulated and as a result, geodesic spectrum is generated.

Table 6.3 Complexity measures of morphologically significant zones decomposed from evolving cloud fields.

Cloud	Zone 1		Zone 2		Zone 3		Zone 4		Zone 5		Zone 6	
	CM	NCM	CM	NCM	CM	NCM	CM	NCM	CM	NCM	CM	NCM
f_1	2.55	0.43	2.79	0.40	2.78	0.40	5.13	0.14	5.02	0.12	0	0
f_2	3.78	0.27	3.77	0.27	5.67	0.10	3.93	0.23	0	0	NA	NA
f_3	4.03	0.24	4.85	0.16	4.49	0.18	4.58	0.17	0	0	NA	NA
f_4	4.29	0.21	5.41	0.12	4.11	0.21	3.60	0.28	0	0	NA	NA
f_5	1.95	0.49	4.33	0.21	5.63	0.10	4.12	0.22	0	0	NA	NA
f_6	2.28	0.46	4.42	0.20	5.72	0.10	3.45	0.27	0	0	NA	NA
f_7	2.96	0.37	4.52	0.19	5.74	0.10	2.96	0.33	0	0	NA	NA
f_8	2.16	0.43	2.29	0.46	5.51	0.11	5.05	0.12	0	0	NA	NA
f_9	4.59	0.18	4.73	0.17	5.50	0.12	0	0	NA	NA	NA	NA
f_{10}	4.64	0.17	4.57	0.17	5.44	0.12	0	0	NA	NA	NA	NA
f_{11}	5.04	0.14	4.85	0.16	5.03	0.15	0	0	NA	NA	NA	NA
f_{12}	5.13	0.13	4.82	0.16	4.84	0.17	0	0	NA	NA	NA	NA
f_{13}	5.51	0.11	4.72	0.16	4.24	0.22	0	0	NA	NA	NA	NA
f_{14}	5.03	0.13	5.27	0.11	3.90	0.26	0	0	NA	NA	NA	NA
f_{15}	4.51	0.15	5.31	0.11	4.38	0.21	0	0	NA	NA	NA	NA

Table 6.4 Details of evolving cloud fields considered with their crossover scales determined, number of decomposed zones, number of geodesic flow fields obtained, and entropy values estimated.

Cloud	Crossover scales	No. dec	No. flow field	Entropy	Cloud	Crossover scales	No. dec	No. flow field	Entropy
f_1	6, 13, 20, 57, 100	6	523 18 48 70 31 243	2.499713 1.031239 1.252941 1.782520 1.327629 2.290906	f_9	25, 53, 100	4	490 128 82 175	2.109592 2.009009 1.750292 2.131398
f_2	14, 28, 83, 100	5	523 43 145 47 239	2.476323 1.409085 2.126950 1.169401 2.326011	f_{10}	27, 54, 100	4	490 70 84 179	2.259992 1.636701 1.810857 2.145319
f_3	17, 48, 73, 100	5	523 50 89 102 159	2.456436 1.553055 1.426105 1.893751 1.931581	f_{11}	36, 67, 100	4	490 138 66 185	2.057739 2.061566 1.677090 2.168453
f_4	20, 67, 87, 100	5	523 91 74 23 432	2.453930 1.781784 1.644839 1.235328 2.579422	f_{12}	40, 71, 100	4	484 139 93 194	1.954383 2.056434 1.716976 2.197023
f_5	4, 25, 81, 100	5	523 105 93 28 265	2.246884 1.711594 1.835823 1.324502 2.360653	f_{13}	51, 81, 100	4	484 172 67 207	1.774722 2.141432 1.566769 2.227641
f_6	5, 27, 87, 100	5	523 74 91 29 275	2.269566 1.642102 1.795090 1.294802 2.374706	f_{14}	38, 85, 100	4	449 304 64 285	1.461633 2.207588 1.476008 2.399226
f_7	8, 32, 91, 100	5	523 74 86 23 281	2.300931 1.613692 1.788957 1.060923 2.385565	f_{15}	30, 79, 100	4	490 148 64 236	1.640367 1.900151 1.591535 2.306958
f_8	5, 10, 58, 100	5	523 74 80 57 167	2.399837 1.197022 1.873356 1.579724 2.123957					

10. Conclusions [1/5]

- Functions and synthetic fractal sets are decomposed into topologically prominent regions and it is found that each decomposed zone possesses varied degree of spatial complexity.

- Multiscale grayscale morphological opening and multiscale binary morphological opening are employed to determine the crossover scales in the sequence of opened versions of sets and/or functions.

- These crossover scales provide the basis to segment the sets and functions of varied complexities involved within. This decomposition process does not involve choosing an arbitrary threshold value.

- The observation in variations in the complexity from one zone to another zone within a set and/or function paves the path to explore links between the growth process and the complexity of each decomposed zone.
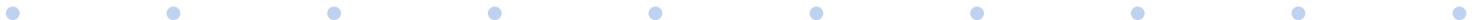
Conclusions [2/5]

- It is observed that each zone that is decomposed from either a function (e.g., digital topographies or cloud fields) or a set possesses a complexity index that varies from zone to zone.

- Such spatial complexity variations are quantified by a host of indices. The loss of information across resolutions is used to compute probability distributions. This loss of information is in terms of lost area of functions where multiscale morphological opening transformation is employed to generate function at multiple resolutions.

- Morphological entropy values are computed for each decomposed zone .

- It is found that each decomposed zone possesses unique morphological entropy. The results obtained are for the two demonstrated cases on synthetic fractal sets and also on clouds retrieved from MODIS satellite data.

Conclusions [3/5]

- The types of transformation that influence the landscape evolution are caused by exodynamic and endodynamic nature.
- Although there is no clear approach to explore whether these two forces that shaped landscape into various forms could be separated out by understanding the degree of convexity of landscape, at least one can explain the stage of the landscape.

Conclusions [4/5]

- Flow fields are generated within topographic and bathymetric basins through geodesic morphological transformations. These flow fields generated are different from that of flow fields usually generated via shallow water equations.

- In reality, topographic and bathymetric undulations which are conspicuous on the surfaces will not be reflected in the flow fields generated using shallow water equations. In the proposed framework, marker and mask are similar to outlet and boundary of threshold elevation region decomposed from geophysical basin.

- The spatial distribution pattern of the regions embedded between the successive flow fields is used to construct geodesic spectra of various basins. Such spectra can be compared with width function that is popular in geomorphology. This approach provides an indicator that has geometric support of surfaces which further provide new characteristics that cannot be unraveled from width function-like metrics.

- The data on which this framework is demonstrated include DEMs and DBMs.

Conclusions [5/5]

- The surficial characterization techniques demonstrated are on static surfaces. However, changes do occur over geophysical surfaces due to perturbations as time goes by.

- Such surfaces where topographic changes are conspicuous across time periods are dynamic surfaces. Hence, the proposed frameworks have also been extended to dynamic surfaces to investigate the characteristics of the changing surfaces.
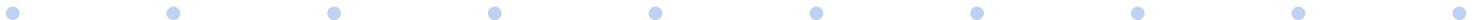
11. Future Work [1/2]

- In this work attempts have been made to show how map algebraic concepts such as mathematical morphology could be employed to segment cloud fields, or generate flow fields within terrestrial basins such as fluvial and tidal basins.

- Specifically, the scope of this entire framework can be foreseen in

    (i) image information mining to retrieve valuable thematic maps,

    (ii) employing those retrieved themes across spatial and temporal scales to understand the occurred changes that are essential to categorize a dynamical system. One such system of terrestrial importance is exogenically sensitive lakes.

    One can make attempts to understand the behavior of such lakes under the influence of perturbations caused due to endogenic and exogenic processes.

Future Work [2/2]

(iii) If such a study gives concrete results, then one can cross check with other dynamical system which is also climatically sensitive.

For instance, tree-rings would provide climate behavioral patterns through which one can understand the fluctuations that occurred in the past in order to understand the future behavior. Although the studies on lakes and tree-rings seem to be independent, it is anticipated that the behavioral patterns of certain variables from the two cases are likely to provide insights in certain process. To carry out such studies, this work provides basic building blocks.

12. References

[1]   Fagherazzi, S., Wiberg, P. L., and Howard, A. D. (2003). *Tidal flow field in a small basin.*   Journal of Geophysical Research, 108(C3), 3071, doi:10.1029/2002JC001340.

[2]   Horton, R. E. (1945). *Erosional development of streams and their drainage basins: Hydrological approach to quantitative morphology.* Bulletin of the Geophysical Society of   America, 56, 275-370.

[3]   Iwanowski, M., and Serra, J. (1999). *Morphological interpolation and color images.* Proceedings of 10th International Conference on Image Analysis and Processing, ICIAP'99.

[4]   Lantuejoul, C., and Maisonneuve, F. (1984). *Geodesic methods in quantitative image analysis.* Pattern Recognition, 17(2), 177-187.

[5]   Maragos, P.A. (1989). *Pattern spectrum and multiscale shape representation.* IEEE Transactions on Pattern Analysis and Machine Intelligence, 11(7), 701-716.

[6]   Maragos, P.A., and Ziff, R. D. (1990). *Threshold superposition in morphological image   analysis system.* IEEE Transactions on Pattern Analysis and Machine Intelligence, 12(5), 498-504.

[7]   Peitgen, H. O., Jürgens, H., and Saupe, D. (2004). *Chaos and Fractals: New Frontiers of Science.* New York: Springer.

[8]   Radhakrishnan, P., Teo, L. L., and Sagar, B. S. D. (2004). *Estimation of fractal dimension through morphological decomposition.* Chaos, Solitons & Fractals, 21(3), 563-572.

[9]   Sagar, B. S. D. (1996*). Fractal relations of a morphological skeleton.* Chaos, Solitons & Fractals, 7(11), 1871-1879.

[10]   Sagar, B. S. D., and Chockalingam, L. (2004). *Fractal dimension of non-network space of a catchment basin.* Geophysical Research Letters, 31(12), L12502.

[11]   Serra, J. (1982). *Image analysis and mathematical morphology.* London: Academic Press.

[12]   Soille, P. (1998). *Grey scale convex hulls: definition, implementation and applications.* Proceedings of the 4th ISMM'98, 83-90.

[13]   Tay, L. T., Sagar, B. S. D., and Chuah, H. T. (2007). *Granulometric analysis of basin-wise DEMs: a comparative study.* International Journal of Remote Sensing, 28(15), 3363-3378.

13. Publication List

[1] Lim, S. L., and Sagar, B. S. D. (2008a). *Cloud field segmentation via multiscale convexity analysis.* Journal of Geophysical Research, 113(D13208), doi:10.1029/2007JD009369.

[2] Lim, S. L., and Sagar, B. S. D. (2008b). *Derivation of geodesic flow fields and spectrum in digital topographic basins*. Discrete Dynamics in Nature and Society, 2008(312870), doi:10.1155/2008/312870.

[3] Lim, S. L., Koo, V. C., and Sagar, B. S. D. (2009). *Computation of complexity measures of morphologically significant zones decomposed from binary fractal sets via multiscale convexity analysis*. Chaos, Solitons & Fractals, 41(3), 1253-1262, doi:10.1016/j.chaos.2008.05.006.

[4] Lim, S. L., Sagar, B. S. D., Koo, V. C., and Tay, L. T. (2010). *Estimation of drainage density from DEM*. Computers & Geosciences (Under review).